6. Sambrotto, R. N. *et al. Nature* **363,** 248–250 (1993).
7. Michaels, A. F., Siegel, D. A., Johnson, R. J., Knap, A. H. & Galloway, J. N. *Global Biogeochem. Cycles* **7,** 339–351 (1993).
8. Sarmiento, J. L., Theile, G., Key, R. M. & Moore, W. S. *J. geophys. Res.* **95,** 18303–18315 (1990).
9. Spitzer, W. S. & Jenkins, W. J. *J. mar. Res.* **47,** 169–196 (1989).
10. Jenkins, W. J. *Nature* **300,** 246–248 (1982).
11. Jenkins, W. J. & Goldman, J. C. *J. mar. Res.* **43,** 465–491 (1985).
12. Jenkins, W. J. *Nature* **331,** 521–523 (1988).
13. Carlson, C. A., Ducklow, H. W. & Michaels, A. F. *Nature* **371,** 405–408 (1994).
14. McCave, I. N. *Deep-Sea Res.* **22,** 491–502 (1984).
15. Bates, N. R., Michaels, A. F. & Knap, A. H. *Mar. Chem.* (submitted).
16. Longhurst, A. R. & Harrison, W. G. *Deep-Sea Res.* **35,** 881–889 (1988).
17. Longhurst, A. R., Bedo, A. W., Harrison, W. G., Head, E. J. H. & Sameoto, D. D. *Deep-Sea Res.* **37,** 685–694 (1990).
18. McClain, C. R. & Firestone, J. *J. geophys. Res.* **98,** 12327–12339 (1993).
19. Keeling, C. D. in *The Global Carbon Cycle* NATO ASI Series I (ed. Heimann, M.) 413–429 (Springer, Berlin, 1993).
20. US JGOFS *Sediment Trap Technology and Sampling* Planning Report 10 1–94 (US JGOFS, Woods Hole, MA, 1989).
21. Eppley, R. W. & Peterson, B. J. *Nature* **282,** 677–680 (1979).
22. Coale, K. H. & Bruland, K. W. *Limnol. Oceanogr.* **32,** 189–200 (1987).
23. Coale, K. H. & Bruland, K. W. *Limnol. Oceanogr.* **30,** 22–33 (1985).
24. Laws, E. A., Ditullio, G. R., Betzer, P. R., Karl, D. M. & Carder, K. L. *Deep-Sea Res.* **36,** 103–120 (1989).
25. Buesseler, K. O. *Nature* **353,** 420–423 (1992).
26. Buesseler, K. O., Michaels, A. F., Siegel, D. A. & Knap, A. H. *Globl Biogeochem. Cycles* **8,** 179–193 (1994).
27. Knauer, G. A., Redalje, D. G., Harrison, W. G. & Karl, D. M. *Deep-Sea Res.* **37,** 1121–1134 (1990).
28. Knauer, G. A. in *Interactions of C, N, P and S Biogeochemical Cycles and Global Change* (eds Wollast, R., MacKenzie, F. T. & Chou, I.) 211–231 (Springer, Berlin, 1993).
29. Karl, D. M. & Knauer, G. A. *Oceanography* **2,** 32–35 (1989).
30. Michaels, A. F., Silver, M. W., Gowing, M. M. & Knauer, G. A. *Deep-Sea Res.* **37,** 1285–1296 (1990).
31. Hansell, D. A. & Newton, J. A. *Limnol. Oceanogr.* **39,** 1487–1495 (1994).
32. Gust, G., Bowles, W., Giordano, S. & Huettel, M. *Aquatic Sciences* (in the press).
33. Martin, J. H., Fitzwater, S. E., Gordon, R. M., Hunter, C. N. & Tanner, S.J. *Deep-Sea Res. II* **40,** 115–134 (1993).
34. Knauer, G. A., Martin, J. H. & Bruland, K. W. *Deep-Sea Res.* **26,** 97–108 (1979).
35. Martin, J. H., Knauer, G. A., Karl, D. M. & Broenkow, W. W. *Deep-Sea Res.* **34,** 267–285 (1987).
36. Worthington, L. V. *The Johns Hopkins Oceanographic Studies* **6,** 1–110 (1976).
37. Platt, T. & Harrison, W. G. *Nature* **318,** 55–58 (1985).

ACKNOWLEDGEMENTS. We thank the BATS technicians R. Sheriff-Dow, R. Johnson, K. Gundersen, J. Sorensen, A. Close, F. Howse, M. Hammer, A. Doyle, M. Best, R. Kelly, F. Bahr and C. Michaels for collecting and processing data, and M. Hartmann for analysing ^{234}Th samples, D. Siegel, D. Hansell, R. Toggweiler, W. Gardner, H. Jannasch, S. Lohrenz and T. Dickey for constructive comments on the manuscript. This research was supported by NSF and NOAA.

A deep earthquake aftershock sequence and implications for the rupture mechanism of deep earthquakes

Douglas A. Wiens*, Jeffrey J. McGuire*, Patrick J. Shore*, Michael G. Bevis†, Kitione Draunidalo‡, Gajendra Prasad‡ & Saimone P. Helu§

* Department of Earth and Planetary Sciences, Washington University, St Louis, Missouri 63130, USA
† Hawaii Institute of Geophysics and Planetology, University of Hawaii, Honolulu, Hawaii 96822, USA
‡ Fiji Mineral Resources Department, Suva, Fiji
§ Tonga Ministry of Lands, Survey, and Natural Resources, Nuku'alofa, Tonga

A distinguishing characteristic of deep earthquakes has been the absence of observable aftershock sequences[1,2]. Here we report the first extensive deep-earthquake aftershock sequence to be observed; it was recorded by an array of eight broadband seismographs following the 9 March 1994 deep Tonga earthquake. The aftershocks show a power-law decay with time following the main shock, as is typical of shallow events. Most of the well located aftershocks are concentrated along a steeply dipping plane consistent with one of the nodal planes of the main-shock mechanism and the mechanisms of three large aftershocks. Assuming these aftershocks denote the main-shock rupture area, they define a 50 × 65 km fault plane extending across the entire width of the active seismic zone and into the surrounding aseismic region. The width of the aftershock zone is wider than the expected width of the metastable olivine wedge, demonstrating that either the width of the metastable olivine material exceeds previous estimates, or the aftershocks are not confined in such a wedge.

It has long been noted that an important difference between deep earthquakes (depth > 300 km) and shallow earthquakes (depth < 70 km) is that the former produce very few aftershocks. Shallow earthquakes are characterized by numerous aftershocks showing an exponential decay with time. A few such aftershock sequences have been reported for intermediate-depth events[3,4], but well developed aftershock sequences have not been observed for deep earthquakes. This difference in aftershock behaviour has been used as primary evidence for a difference in earthquake generating mechanisms between shallow and deep earthquakes[1,2,5,6]. The lack of aftershocks for deep earthquakes has also prevented delineation of the rupture zones of large, deep earthquakes. Previous studies suggest that the few observed deep-earthquake aftershocks do not seem to cluster along the fault planes of the main shocks[7], as aftershocks do for shallow events.

The 9 March 1994 (moment magnitude $M_w = 7.6$; depth, 564 km) earthquake in the Tonga slab was larger than any deep earthquake during the previous 20 years. This earthquake was followed by an unprecedented aftershock sequence, which exceeds the number of aftershocks of all deep earthquakes during the past 35 years (Table 1), including the recent deep Bolivia earthquake ($M_w = 8.3$)[8], the largest deep earthquake ever recorded. In addition, the deep Tonga earthquake occurred beneath an array of portable digital broadband seismographs installed in Tonga, Fiji and Niue Island (Fig. 1) which enables detailed study of the locations and focal mechanisms of the after-

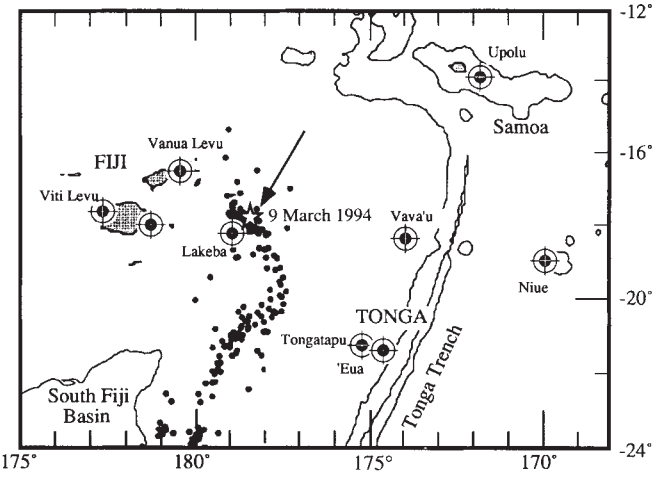

FIG 1. Map of the southwest Pacific showing the location of the 9 March 1994 deep Tonga earthquake (star) and the locations of regional digital broadband seismic stations (large black dots with cross). All stations are part of a temporary network deployed in late 1993 except for Samoa, which is a permanent IRIS station. The 4,000-m and 8,000-m bathymetric contours are shown, along with the locations of a 2-year sample of deep earthquakes in the Tonga slab (small black dots). Seismograph locations are denoted by the island name. The arrow shows the strike of the steeply dipping fault plane of the 9 March event, as determined from the aftershock distribution.

TABLE 1 Aftershocks of large deep earthquakes, 1960–94

Date	Location	M_w	Depth	Number of aftershocks		
				$m_b \geq 5.0$	$m_b \geq 4.5$	Total
15 Aug. 1963	Peru	7.8	543	0	0	0
11 Nov. 1963	Peru	7.6	600	1	2	5
7 Oct. 1968	Izu–Bonin	7.4	457	0	1	1
31 July 1970	Columbia	8.2	653	0	0	0
30 Aug. 1970	Sea of Okhotsk	7.3	643	0	0	0
29 Sept. 1973	Sea of Japan	7.8	567	0	0	0
22 June 1982	Banda Sea	7.4	450	0	0	0
6 Mar. 1984	Izu–Bonin	7.4	457	0	1	2
9 Mar. 1994	Tonga–Fiji	7.6	564	11	40	82
9 June 1994	Bolivia	8.3	636	1	—	36

Earthquakes include all events 300–700 km deep with seismic moment $>1 \times 10^{20}$ Nm, from Abe[29] and the Harvard centroid moment tensor catalogue[30]. Aftershock data is from the International Seismological Centre, Newbury, UK, except for the 1994 Tonga data which are from the monthly Preliminary Determination of Epicenters (PDE; US Geological Survey) and the regional network, and the 1994 Bolivia data which are from the weekly PDE and Myers *et al.*[8]. The total number of aftershocks is biased by different detection thresholds, but detection should be uniform at the body-wave magnitude $m_b = 5.0$ level. (M_w, moment magnitude.)

shocks. This array recorded a sequence of 82 aftershocks that extended for at least 42 days and ranged in body-wave magnitude (m_b) from 3.8 to 6.0. Many more probable aftershocks were visible on the records of the two best stations during the initial hours after the main shock.

The aftershocks show a rapid power-law decay with time (Fig. 2), as is observed for the aftershock sequences of shallow earthquakes[9–11]. We fitted the time distribution of the aftershocks using a maximum-likelihood fit to the modified Omori relationship[12,13] $N(t) = K(t+c)^{-p}$, where $N(t)$ is the number of earthquakes per unit time and K, c and p are empirical constants. This relation provides a good fit to the decay rate (Fig. 2), with $p = 1.0$ giving the optimum fit. This is identical to the average p value for shallow earthquake sequences[10,11], suggesting similarities in the aftershock generating process between deep and shallow earthquakes. But it differs from the only previously suggested p value for deep earthquakes, $p = 0.54$, obtained from superposition of data from many earthquakes which individually had too few aftershocks to obtain a result[11].

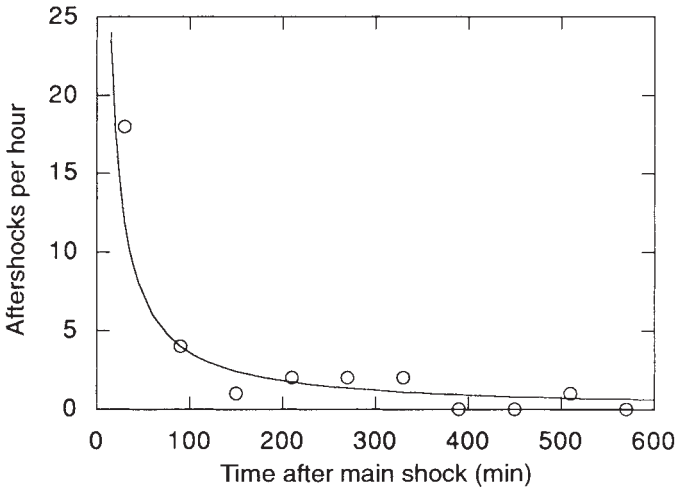

FIG. 2 Plot of the number of aftershocks per hour (open circles) as a function of time after the main shock. Also shown is a line representing the maximum-likelihood fit to the modified Omori relationship[12,13] of the aftershock times from the first 18 days of the sequence. The aftershock decay is best fitted by a power-law decay with exponent $p = 1$, similar to aftershock sequences of shallow earthquakes.

We determine the relative positions and uncertainties of the main shock and aftershocks by inverting P and S phases from the regional network along with teleseismic P, pP and PKP phases using a hypocentroidal decomposition algorithm[14]. This method uses arrival times from different earthquakes at the same station to constrain earthquake relative positions within a limited source region, thus minimizing the effect of velocity heterogeneity along the ray paths. The results are displayed and analysed using a three-dimensional graphics package which renders the 95% confidence volumes of the earthquake locations as geometric solids[15].

The main shock and 14 out of 18 well located aftershocks are localized along a nearly vertical plane (Fig. 3*a*). Three well located aftershocks not displayed in Fig. 3*a* were located at least 70 km from the main shock hypocentre and seem unlikely to be part of the main-shock rupture zone. The plane that has the best least-squares fit to the locations of nine aftershocks that occurred during the first day following the main event has strike 30°, dip 68°, and the maximum distance of any of the events from the plane is 5 km.

This plane is in good agreement with a steeply dipping NNE-striking nodal plane in the focal mechanism of the main shock (Fig. 4 top). Focal mechanisms were determined by inverting the regional and teleseismic body waveforms using synthetics calculated with a reflectivity method[16,17]. The result shows a north–south striking, steeply dipping fault plane (strike 5°, dip 70°), and is nearly identical to the Harvard centroid moment tensor solution for the main shock (G. Ekstrom and A. Dziewonski, personal communication). This plane deviates by 25° in strike from the plane determined from the aftershock locations. There is, however, considerable evidence for a change in focal mechanism as the rupture progressed, including changes in the polarity of broadband-displacement P and S waves during the rupture pulse and the results of preliminary studies of the main-shock rupture process[18] (M. Kikuchi, personal communication). Also plotted in Fig. 4 (top) is a focal mechanism determined solely from P and S wave first motions; it differs by only 5° in strike and 4° in dip from the plane determined from the aftershock locations, demonstrating that the aftershock plane is consistent with the focal mechanism of the first part of the main-shock rupture.

Broadband displacement waveforms from the regional array were also inverted for the focal mechanisms of some of the larger aftershocks (Fig. 4 bottom). These events showed focal mechanisms similar to that of the main shock, with steeply dipping fault planes roughly consistent with the planar distribution of aftershocks. The strike of the steeply dipping fault plane varies from 10° to 45°, suggesting some variability in fault strike.

Within the planar region, the aftershocks concentrate near the epicentre of the main shock, but they seem to delineate a rupture zone of $\sim 50 \times 65$ km (Fig. 3*b*). This rupture dimension is consistent with that expected for an earthquake of this magnitude, and combined with the observed rupture duration of ~14 s (ref. 18) suggests a rupture velocity of ~ 2.5 km s^{-1}. If the main shock ruptured through the entire region defined by the aftershocks, this suggests a stress drop of ~1.6 MPa (16 bar), consistent with previous suggestions that deep earthquakes show similar stress drops to shallow earthquakes[19,20].

To investigate the spatial relationship between the rupture zone of the 9 March event and the Tonga deep seismic zone, we inverted for the positions of the well located aftershocks relative to teleseismically recorded earthquakes in this region using the same relocation method. The fault plane defined by the aftershocks of the 9 March event is nearly vertical and cuts across the seismically active slab, extending entirely across the thickness (~30 km) of the active seismic zone (Fig. 3*c*). Two events occur outside the active zone, as defined by the previous seismicity. These event locations are well constrained and the one to the

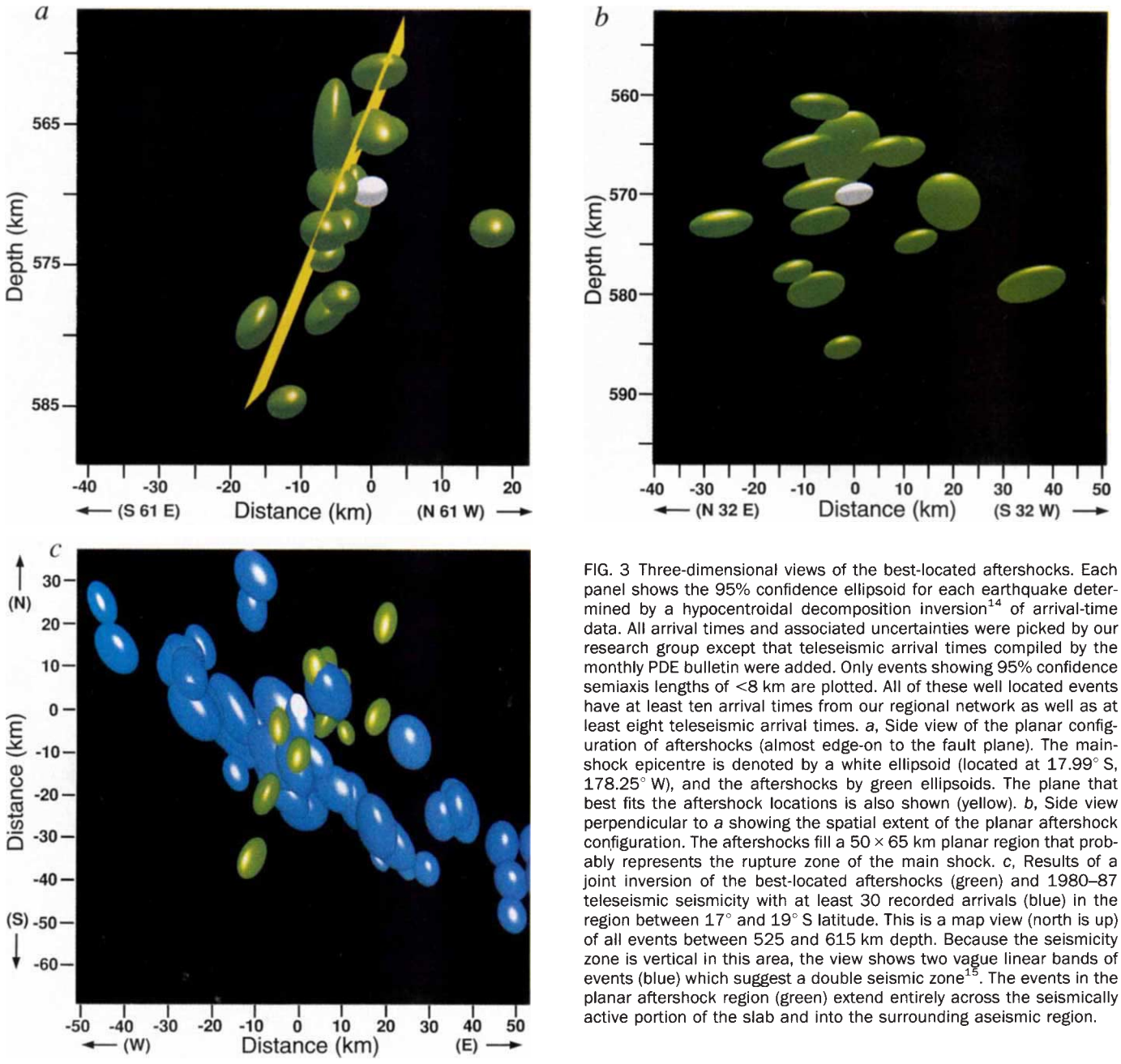

FIG. 3 Three-dimensional views of the best-located aftershocks. Each panel shows the 95% confidence ellipsoid for each earthquake determined by a hypocentroidal decomposition inversion[14] of arrival-time data. All arrival times and associated uncertainties were picked by our research group except that teleseismic arrival times compiled by the monthly PDE bulletin were added. Only events showing 95% confidence semiaxis lengths of <8 km are plotted. All of these well located events have at least ten arrival times from our regional network as well as at least eight teleseismic arrival times. *a*, Side view of the planar configuration of aftershocks (almost edge-on to the fault plane). The mainshock epicentre is denoted by a white ellipsoid (located at 17.99° S, 178.25° W), and the aftershocks by green ellipsoids. The plane that best fits the aftershock locations is also shown (yellow). *b*, Side view perpendicular to *a* showing the spatial extent of the planar aftershock configuration. The aftershocks fill a 50 × 65 km planar region that probably represents the rupture zone of the main shock. *c*, Results of a joint inversion of the best-located aftershocks (green) and 1980–87 teleseismic seismicity with at least 30 recorded arrivals (blue) in the region between 17° and 19° S latitude. This is a map view (north is up) of all events between 525 and 615 km depth. Because the seismicity zone is vertical in this area, the view shows two vague linear bands of events (blue) which suggest a double seismic zone[15]. The events in the planar aftershock region (green) extend entirely across the seismically active portion of the slab and into the surrounding aseismic region.

FIG. 4 Focal mechanisms of the 9 March 1994 deep Tonga earthquake and larger aftershocks. Top, lower-focal-hemisphere projection of the main shock determined from first motions (short dashed lines) and from inversion of regional and teleseismic long-period three-component data (solid lines). The orientation of the plane which best fits the well located aftershocks that occurred during the first day after the main shock is also shown (long dashes). The difference between the first-motion mechanism and the long-period inversion suggests changes in the focal mechanism during the rupture, with the steeply dipping plane of the first motion mechanism showing excellent agreement with the plane determined from the alignment of aftershocks. Bottom, source mechanisms determined for the larger aftershocks from inversion of regional three-component data. All the mechanisms display steeply dipping north- to northeast-striking fault planes consistent with the main-shock focal mechanism and the alignment of aftershocks, but with some variability indicating heterogeneity in fault orientation. The 27 March 1994 event, located outside the active slab as defined by the background seismicity (Fig. 3c), shows a focal mechanism nearly identical to that of the main shock.

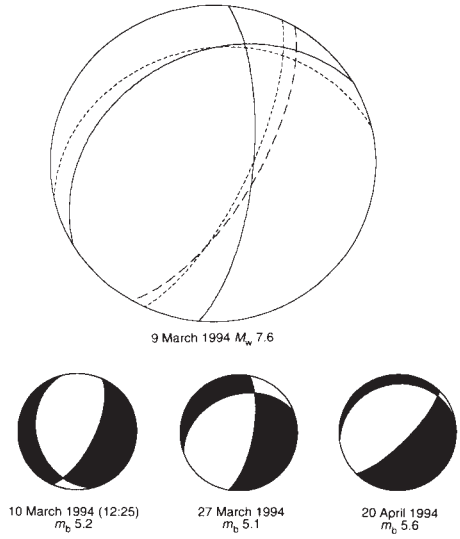

north, on 27 March, shows a focal mechanism similar to that of the main shock (Fig. 4 bottom). This suggests that the main-shock rupture may have propagated beyond the limits of the background seismicity in this region, or at least triggered aftershocks within the normally aseismic region surrounding the seismically active slab.

Recent research suggests that deep earthquakes may be caused by transformational faulting, as material within a wedge of metastable olivine[21,23] is transformed to a spinel structure[5,6,24,25]. Because the transformation is temperature-activated, deep earthquakes should occur preferentially in the warmer, outer regions of the metastable wedge, possible forming a double seismic zone[15,26]. The background seismicity near the 9 March event, when viewed in cross-section, shows two rather indistinct vertical alignments of earthquakes along the edges of the slab that may represent such a double seismic zone (blue ellipses in Fig. 3*c*).

The zone of aftershocks of the 9 March event cuts across the entire zone of seismicity and some distance into the surrounding aseismic region, extending for at least 55 km in a direction perpendicular to slab strike. Although it may be possible that the main-shock rupture did not extend all the way to the outer aftershocks, the two aftershocks unmistakably initiated outside the normal zone of seismicity. The 55 km width of the aftershock zone exceeds both the width of the background seismicity in the slab (Fig. 3*c*) and current estimates of the width of the metastable wedge[15,27] based on slab thermal models[28] and the kinetics of the olivine–spinel reaction[21,23] (~20 km at this depth in the Tonga slab). We propose that either the metastable olivine wedge is much wider than previously thought, because of deficiencies in the thermal models or kinetic calculations, or that the aftershocks are not confined within such a wedge. The first option seems unlikely, as it requires an explanation for the confinement of the background seismicity to a zone much narrower than the metastable wedge. If the aftershocks are occurring outside the zone of metastable olivine, then a mechanism for their occurrence other than transformational faulting must be sought. □

Received 29 August; accepted 15 November 1994.

1. Leith, A. & Sharpe, J. A. *J. Geol.* **44,** 877–917 (1936).
2. Frohlich, C. *A. Rev. Earth planet. Sci.* **17,** 227–254 (1989).
3. Pavlis, G. L. & Hamburger, M. W. *J. geophys. Res.* **96,** 18107–18117 (1991).
4. Kisslinger, C. & Hasegawa, A. *Tectonophysics* **197,** 27–40 (1991).
5. Green, H. W. & Burnley, P. C. *Nature* **341,** 733–737 (1989).
6. Kirby, S. H., Durham, W. B. & Stern, L. A. *Science* **252,** 216–225 (1991).
7. Willemann, R. J. & Frohlich, C. *J. geophys. Res.* **92,** 13927–13943 (1987).
8. Myers, S. C. *et al. Geophys. Res. Lett.* (in the press).
9. Omori, F. *J. Coll. Sci. Imp. Univ. Tokyo* **7,** 111–200 (1895).
10. Kisslinger, C. & Jones, L. M. *J. geophys. Res.* **96,** 11947–11958 (1991).
11. Davis, S. D. & Frohlich, C. *J. Geophys. Res.* **96,** 6335–6350 (1991).
12. Utsu, T. *Geophys. Mag.* **30,** 521–605 (1961).
13. Ogata, Y. *J. Phys. Earth* **31,** 115–124 (1983).
14. Jordan, T. H. & Sverdrup, K. A. *Bull. seism. Soc. Am.* **71,** 1105–1130 (1981).
15. Wiens, D. A., McGuire, J. J. & Shore, P. J. *Nature* **364,** 790–793 (1993).
16. Fuchs, K. & Muller, G. *Geophys. J. R. astr. Soc.* **23,** 417–433 (1971).
17. Kennett, B. L. N. *Seismic Wave Propagation in Stratified Media* (Cambridge Univ. Press, 1983).
18. McGuire, J. J. *et al.* (abstr.) *EOS* **75,** 466 (1994).
19. Wyss, M. & Molnar, P. *Phys. Earth planet. Inter.* **6,** 279–292 (1972).
20. Houston, H. & Williams, Q. *Nature* **352,** 520–522 (1991).
21. Sung, C. & Burns, R. G. *Tectonophysics* **31,** 1–32 (1976).
22. Iidaka, T. & Suetsugu, D. *Nature* **356,** 593–595 (1992).
23. Rubie, D. C. & Ross, C. R. *Phys. Earth planet Inter.* (in the press).
24. Kirby, S. H. *J. geophys. Res.* **92,** 13789–13800 (1987).
25. Green, H. W., Young, T. E., Walker, D. & Scholz, C. H. *Nature* **348,** 720–722 (1990).
26. Iidaka, T. & Furukawa, Y. *Science* **263,** 1116–1118 (1994).
27. Stein, S., Kirby, S. H., Rubie, D. & Okal, E. A. paper presented at the SUBCON conference, Avalon, California, 13–17 June 1994.
28. Toksoz, M. N., Sleep, N. H. & Smith, A. T. *Geophys. J. R. astr. Soc.* **35,** 285–310 (1973).
29. Abe, K. *J. Phys. Earth* **30,** 321–330 (1982).
30. Dziewonski, A. M., Chou, T. & Woodhouse, J. H. *J. geophys. Res.* **86,** 2825–2852 (1981).

ACKNOWLEDGEMENTS. Equipment for this research was obtained from the PASSCAL programme of the Incorporated Research Institutes in Seismology. We thank G. Hade and P. Friberg for assistance in deploying the seismographs. We also thank R. van der Hilst for providing data from seismic stations in the Australian SKIPPY deployment, D. Rouland and R. Pillet for providing data from stations in Vanuatu and New Caledonia, T. Wallace for a copy of his paper before publication, and B. Park-Li and R. Sakata for picking phase arrival times. The manuscript was improved by reviews from J. Vidale and H. Green. This work was supported by the US NSF.

Combined spatial and temporal imaging of brain activity during visual selective attention in humans

H. J. Heinze*†, G. R. Mangun†‡, W. Burchert§, H. Hinrichs*, M. Scholz*, T. F. Münte‖, A. Gös‖, M. Scherg‖, S. Johannes‖, H. Hundeshagen§, M. S. Gazzaniga‡ & S. A. Hillyard#

* Department of Clinical Neurophysiology, Otto-v-Guericke University, D-39120 Magdeburg, Germany
‡ Department of Psychology and Center for Neuroscience, University of California at Davis, Davis, California 95616, USA
§ Department of Nuclear Medicine, Medical School of Hannover, 3000 Hannover, Germany
‖ Department of Neurology, Medical School of Hannover, 3000 Hannover, Germany
‖ Department of Neurology, University of Heidelberg, Heidelberg, Germany
Department of Neurosciences, University of California at San Diego, La Jolla, California 92093, USA

VISUAL-SPATIAL attention is an essential brain function that enables us to select and preferentially process high priority information in the visual fields[1,2]. Several brain areas have been shown to participate in the control of spatial attention in humans[3–5], but little is known about the underlying selection mechanisms. Non-invasive scalp recordings of event-related potentials (e.r.ps) in humans have shown that attended visual stimuli are preferentially selected as early as 80–90 ms after stimulus onset[6,7], but current e.r.p. methods do not permit a precise localization of the participating cortical areas. In this study we combined neuroimaging (positron emission tomography) with e.r.p. recording in order to describe both the cortical anatomy and time course of attentional selection processes. Together these methods showed that visual inputs from attended locations receive enhanced processing in the extrastriate cortex (fusiform gyrus) at 80–130 ms after stimulus onset. These findings reinforce early selection models of attention[8–10].

In our spatial attention task, healthy young subjects ($N = 10$) attended selectively to the right or left half of bilateral stimulus arrays that were flashed in rapid sequence (Fig. 1, top). Attention was directed covertly while the subjects' gaze remained fixated on a central dot; fixation was verified with both electro-oculographic and high-resolution infrared video methods. Changes in regional cerebral blood flow (activation) as a function of selective attention were measured using the positron emission tomography (PET) $H_2{}^{15}O$ method. These activations were first visualized as difference images derived by subtracting the images obtained during passive viewing from those obtained in the attend-left or the attend-right conditions (Fig. 1). Focused attention produced significant PET activation in the hemisphere contralateral to the attended visual hemifield (Table 1). Specifically, attending to the left produced a significant activation in the right posterior fusiform gyrus of extrastriate visual cortex (Fig. 1, left column), whereas attending to the right produced activation in the left fusiform gyrus (Fig. 1, right column).

Significant activations were also obtained in the right anterior cingulate gyrus, and left superior frontal gyrus for the attend-left minus passive PET images (Table 1). Significant activations in the thalamus reached statistical significance only for the attend-right minus passive subtraction (Fig. 1). No significant attention-related activations were obtained in the striate cortex or parietal cortex in this task.

† To whom correspondence should be addressed.